



Rapid quantitative analysis of trace elements in plutonium alloys using a handheld laser-induced breakdown spectroscopy (LIBS) device coupled with chemometrics and machine learning

Journal:	<i>Analytical Methods</i>
Manuscript ID	AY-ART-05-2021-000826.R1
Article Type:	Paper
Date Submitted by the Author:	16-Jun-2021
Complete List of Authors:	Rao, Ashwin; Air Force Institute of Technology, Jenkins, Phillip; Air Force Institute of Technology, Vu, Dung; Los Alamos National Laboratory, C-PCS Auxier, John; Los Alamos National Laboratory, Actinide Analytical Chemistry Patnaik, Anil; Air Force Institute of Technology Shattan, Michael; Air Force Institute of Technology, Dept of Engineering Physics;

Journal Name

ARTICLE TYPE

Cite this: DOI: 00.0000/xxxxxxxxxx

Rapid quantitative analysis of trace elements in plutonium alloys using a handheld laser-induced breakdown spectroscopy (LIBS) device coupled with chemometrics and machine learning

Ashwin P. Rao,^a Phillip R. Jenkins,^a Dung M. Vu,^b John D. Auxier II,^b Anil K. Patnaik,^a and Michael B. Shattan^{*a}

Received Date

Accepted Date

DOI: 00.0000/xxxxxxxxxx

We present the first reported quantification of trace elements in plutonium via a portable laser-induced breakdown spectroscopy (LIBS) device and demonstrate the use of chemometric analysis to enhance the handheld device's sensitivity and precision. Quantification of trace elements such as iron and nickel in plutonium metal via LIBS is a challenging problem due to the complex nature of the plutonium optical emission spectra. While rapid analysis of plutonium alloys has been demonstrated using portable LIBS devices, such as the SciAps Z300, their detection limits for trace elements are severely constrained by their achievable pulse power and length, light collection optics, and detectors. In this paper, analytical methods are evaluated as a means to circumvent the detection constraints. Three chemometric methods often used in analytical spectroscopy are evaluated; principal component regression, partial least-squares regression, and artificial neural networks. These models are evaluated based on goodness-of-fit metrics, root mean-squared error, and their achievable limits of detection (LoDs). Partial least squares proved superior for determining content of iron and nickel in plutonium metal, yielding LoDs of 15 and 20 ppm, respectively. These results of identifying the undesirable trace elements in plutonium components are critical for applications such as fabricating radioisotope thermoelectric generators or nuclear fuel.

1 Introduction

Multivariate and machine learning methods are commonplace in modern spectroscopic analysis; these tools provide significant advantages in analyzing complex spectra and producing accurate classification or regression models from spectroscopic data^{1,2}. The application of these methods for the purposes of chemical analysis is known as chemometrics. The most widely-used chemometric techniques for improved elemental analysis and sample discrimination are principal components analysis (PCA)^{3–6}, partial-least squares (PLS)^{7–10} and artificial neural networks (ANNs)^{11–14}. These techniques can yield marked improvements in LoDs for determining elemental concentrations in a bulk substrate when compared to traditional univariate analysis^{15–17}. PCA and PLS are dimensionality reduction techniques which can be used to deconstruct a data set into a representative model with less variables than present in the original¹⁸. ANNs are often used

to ascertain complex relationships among different variables in large data sets. These techniques have demonstrated significant use in the creation of chemical analysis models from spectra of geological¹⁹, ore²⁰, pharmaceutical²¹ and Martian rock samples²². Additionally, these methods have also successfully been applied to increase precision and sensitivity of regression models predicting Si content in plutonium surrogate material²³.

This paper focuses on taking advantage of such analytical methods for trace element quantification in plutonium (Pu) alloys. The processing of Pu metal for nuclear component production is an amalgamation of several complex chemical and metallurgical techniques^{24–26}. These processes introduce many avenues for trace metal impurities, such as iron and nickel, to leach into the plutonium metal²⁷. These elements are known to lower the melting point of plutonium and form a low-melting eutectic, affecting the stability of the Pu phase structure and could lead to component failure in higher temperature applications^{26,28–30}, also trace element build up could dramatically change the reaction cross section. Monitoring of trace element concentrations in plutonium is typically conducted via inductively coupled plasma-mass spectroscopy (ICP-MS) and inductively coupled plasma-optical emis-

* Corresponding Author

^a Air Force Institute of Technology, 2950 Hobson Way, WPAFB, OH 45424, USA. E-mail: michael.shattan@afit.edu

^b Actinide Analytical Chemistry, Chemistry Division, Los Alamos National Laboratory, Los Alamos, NM 87545

sion spectroscopy (ICP-OES)³¹. Both techniques yield accurate determinations of elemental impurities with low limits of detection (LoDs) in fractions of parts-per-million (ppm)^{32,33}. Although ICP methods are reliable and well-established, there are serious limitations in large-scale implementations; e.g., 1) these techniques require an extensive sample preparation process, often involving acid digestion of the plutonium metal over periods of several hours; 2) the size of the equipment prevents this analysis from being conducted *in-situ*, and Pu samples must be moved between labs for impurity analysis^{34,35}. To circumvent these limitations, we propose to develop new analytical methods implemented in tandem with a portable device to conduct instantaneous, *in-situ* trace element measurements of Pu metal at various stages in the production process.

One technique that shows promise for meeting the aforementioned criteria is laser-induced breakdown spectroscopy (LIBS)^{36,37}. LIBS is a versatile technique and has been demonstrated for analytical use in a wide range of fields such as soil^{38,39} and geological^{22,40} analysis, food science⁴¹, industrial hygiene⁴² and combustion diagnostics^{43,44}. Portable, handheld LIBS devices are sold commercially and marketed for industrial and scrap metal analysis⁴⁵. Although these devices are not advertised for nuclear material analysis, recent studies have proven them effective for quantification of uranyl fluoride contamination⁴⁶, rare earth metals in uranium matrices⁴⁷, and trace elements in plutonium surrogates⁴⁸. Two metrics which can determine efficacy of the handheld LIBS device for trace metal analysis are root mean-squared error (*RMSE*) and LoD. *RMSE* pertains to the precision and accuracy of predictive models created using data taken by the handheld device. This statistical measure quantifies the average of the square of errors generated by a prediction model. LoD is a measure of the sensitivity of a generated model to changes in the recorded spectra – expressed in units of concentration (or amount), that describes the lowest concentration level (or amount) of the element that an analyst can determine to be statistically different from an analytical blank⁴⁹. SciAps reports nominal LoD values for common metal impurities such as iron and nickel at 500 ppm using their Z series LIBS analyzers, whereas others such as copper, aluminium, sodium and silicon range between 100-200 ppm. Previous work by Shattan et al. demonstrated an LoD of 250 ppm for uranium on stainless steel⁴⁶. For effective trace metal content determination in Pu, these LoDs must be improved beyond the factory value to the low 100s or even 10s of ppm, highlighting the need to implement chemometrics to improve model sensitivity.

This work represents the first investigation of its kind on plutonium combining advanced analytical methods and a portable analytical device. Spectra taken of Pu samples from a SciAps Z300 portable LIBS device are used to train and test different regression techniques. PCA, PLS, and ANN methods are used to generate regression models from the spectral data; the regression fits, *RMSEs*, and LoDs of each model are evaluated to determine analytical performance and predictive capability of each chosen method. It is demonstrated that by employing the chemometric or machine-learning based analytical methods, the LoD of trace metals in Pu sample could reach sub-hundred ppm levels using

the handheld LIBS device, comparable to the sensitivity achieved in full laboratory-scale setups.

In this paper, the handheld LIBS based experiment is described in Section 2; the analytical methods used for comparisons are presented in Sec 3. In section 4, the results and detailed discussions on analysis of the LIBS data is presented for trace element quantification in Pu alloy and LoD is determined. The summary and conclusions are presented in Section 5.

2 Experimental

2.1 Samples



Fig. 1 Notional image of size of Pu coupon samples used in this study.

The Pu samples used in this study were metal coupons approximately 30 mm in diameter; a notional depiction is presented in Fig. 1. These samples had varying concentrations of the two trace elements analyzed in this study. The sample compositions are listed in Table 1. Due to radioactivity and pyrophoricity of plutonium metal, our work had limited access to only a few different Pu samples for spectroscopic introspection. However, a large amount of spectra were recorded from each sample to ensure sufficient data for constructing chemometric models. The first sample, labeled S0, was a plutonium Certified Reference Material (CRM) at 99.96% purity. The other samples were fabricated alloys with different levels of various trace elements present. The concentrations of several trace elements in these samples were verified by ICP methods at LANL, and we were provided the concentrations of Fe and Ni for this study. Additionally, samples 3 and 4 have the same reported concentrations for both metals as these two sample pieces originated from the same larger component. They were removed to initially analyze alloy homogeneity.

Table 1 Trace element concentrations of each type of sample used in Pu spectral data acquisition.

Sample type	Trace element content (ppm)	
	Fe	Ni
S0	0	0
S1	634	1305
S2	743	561
S3	246	105
S4	246	105

2.2 Portable LIBS instrument

A SciAps Z300 handheld LIBS analyzer (Fig. 2) was used for spectral acquisition, and was placed in the Ar controlled glovebox with the Pu samples. A 5 mJ per pulse at 1064 nm Nd:YAG laser

with a repetition rate of 50 Hz and 1.5 cm focal length is used in the Z300 to produce the microplasma. Optical emissions are collected by three onboard spectrometers and recorded on a CCD detector, rendering a spectrum from 180-960 nm. An example Pu spectra recorded by the device is illustrated in Fig. 3, with the major Pu and Ar emission peaks labeled. Spectral acquisition



Fig. 2 SciAps Z300 LIBS analyzer.

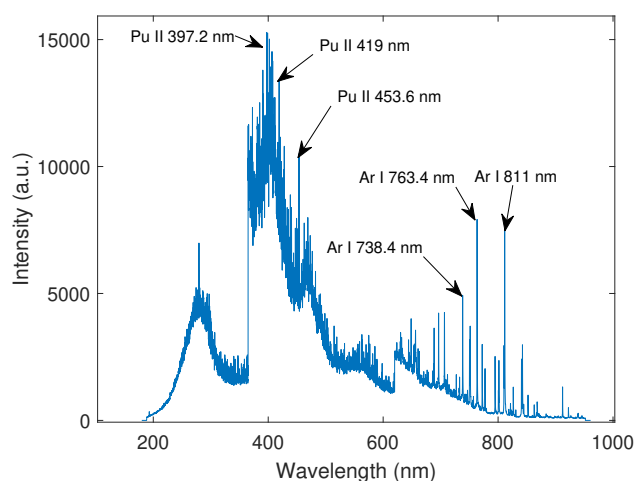


Fig. 3 Pu CRM sample spectra recorded by Z300.

was conducted through the SciAps Profile Builder software, enabling laser triggering and data acquisition settings changes from the computer, while the device remained in glovebox. The device was used in gated collection mode, with a gate delay of 250 ns and an integration period of 1 ms. An 8x8 raster pattern was implemented, recording 8 spectra at 8 locations on the sample each time the laser was triggered and averaging every 8 spectra, yielding a final total of 8 spectra per individual recording. Between 2-6 locations on each sample were tested, generating a total of 145 spectra collected across the whole sample set after a few individual spectra were thrown out due to recording errors by the computer software. It should be noted that while the device is triggered from an external laptop, it is held to the sample by a glovebox operator. Small hand movements during the laser firing and signal recording process can yield jitter and shot-to-shot deviations in the spectra that are greater than a typical labora-

tory LIBS experiment. This was partially mitigated by operator training, and our work yielded shot-to-shot intensity fluctuations of 30% which is within the typical range for LIBS experiments; this was adjusted for during pre-processing using the standard normal variate (SNV) method for spectral normalization. SNV is commonly implemented in pre-processing of LIBS, Raman, and near-infrared (NIR) spectra to reduce signal fluctuation and yield enhanced analytical performance^{8,50,51}. The SNV method is depicted in Eq. 1. Each spectrum (I_k) is centered on its mean value (μ_I) and then divided by the original spectrum standard deviation to yield the SNV normalized spectrum (I_k^{snv}).

$$I_k^{snv} = \frac{I_k - \mu_I}{\sigma_I}, \quad \forall k \quad (1)$$

Chemometric routines were developed to utilize the entire UV-VIS spectra to identify changes in analyte concentration and compared to a univariate technique based on a singular peak height. The overarching goal of implementing chemometrics in this work was to generate a robust prediction model that can relate holistic changes across the breadth of the UV-VIS spectra that are related to changes in analyte concentration. Chemometric methods are imperative when analyzing a complex metal like plutonium due to the large amount of spectral interferences that can occur with other trace analytes in the sample. This is illustrated in Figs. 4 and 5, which demonstrate the close proximity or direct interference of common Fe and Ni emissions with nearby Pu emission lines. These large interferences between emissions of the bulk and trace analyte material throughout the spectra make traditional univariate calibration methods difficult to implement for development of accurate regression models. The complexity of the spectra of actinide metals therefore highlights the need for more advanced techniques which can adequately detect peaks of trace metals like Ni and Fe and discern the relationship between small changes in spectral intensity and the trace analyte concentration.

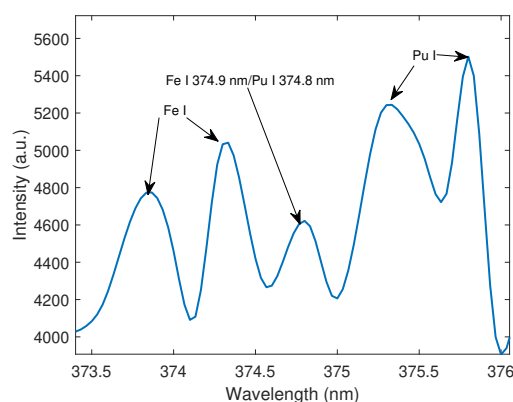


Fig. 4 Fe lines around 373-374 nm and surrounding Pu I emissions.

3 Description of analytical methods

3.1 Univariate analysis

Univariate analysis generates a simple regression model relating changes in intensity of an emission line, or intensity ratios of

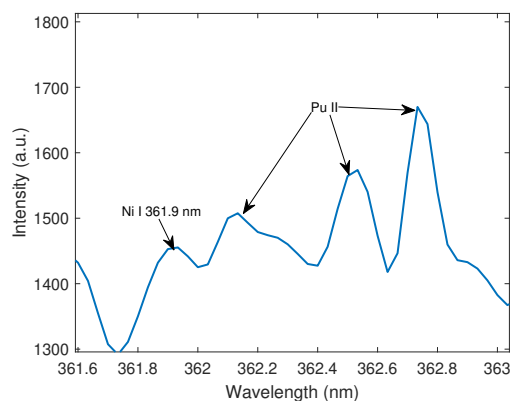


Fig. 5 Ni I 361.9 nm line and nearby Pu II interferences.

emission lines, to changes in analyte concentration across a sample set. A simple linear regression fit to these data points generates a calibration curve describing the sensitivity of the spectral response to the concentration. The univariate calibration method works best when the emission line of interest can be extracted from a simple, well-resolved spectrum without interferences from other nearby emissions. LoDs based on univariate calibrations are directly dependent on the sensitivity (slope) of the calibration; this often results in univariate calibrations plagued by imprecision and lower accuracy when applied to complex spectra.

3.2 Principal component analysis (PCA)

PCA is an unsupervised dimensionality reduction technique, used to transform an original data set into a smaller group of variables called components, without relating them to any output variables. Each component explains some percentage of the variance of the original input data. The principal components are comprised of two types of transformed variables; scores and loadings. Loadings describe correlations between input variables and their contributions to the data set. Scores quantify patterns and correlations between the samples in the data set itself. PCA is particularly useful in analytical spectroscopy to reduce the complexity of the data set into something more easily interpretable. Loadings of the different spectral wavelengths can pinpoint which emissions are responsible for variance in the data set, whereas scores can be used to cluster samples based on bulk similarities. For example, in a previous study using a SciAps Z500 for analysis of cerium alloys PC scores were used to cluster the samples based on their gallium content⁵².

3.3 Partial least-squares (PLS)

PLS is a supervised dimensionality reduction technique, often used to simplify analysis of large data sets². The method transforms raw input data into a smaller set of data called latent variables (LVs), which describe most of the variance of the original data. The LVs can then be utilized for visual clustering analysis, or to create mathematical regression models. This process is depicted in Fig. 6. PLS differs from PCA by generating data accounting for the covariance between input and output variables. This

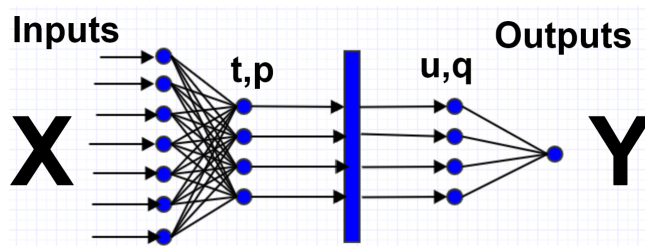


Fig. 6 Flowchart of PLS decomposition. Latent variables and weight loadings (t, p) are calculated from input data. These are then used to calculate latent variables and loadings (u, q) relating the decomposed input (X) to the output (Y).

often yields higher accuracy regression models from large data sets¹⁸; the PLS algorithm can thus provide significant advantages over PCA when trying to relate small changes in a complex spectral response to changes in trace element content among samples.

3.4 Artificial Neural Networks (ANNs)

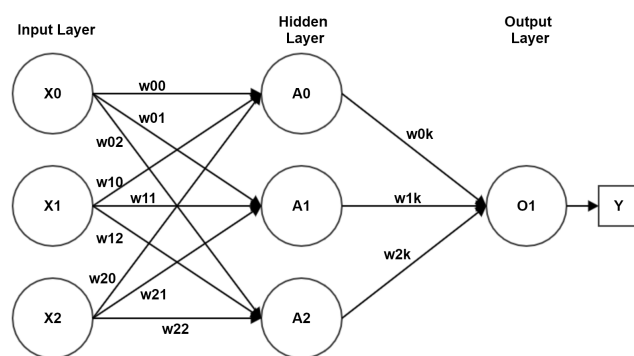


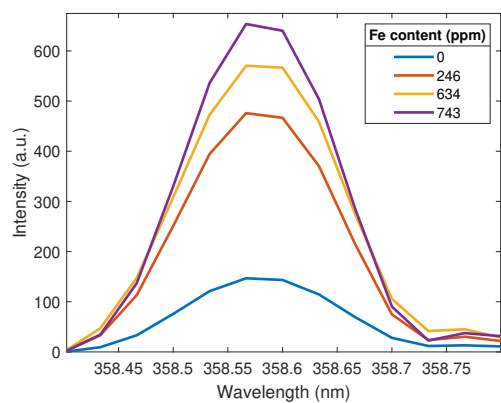
Fig. 7 ANN architecture diagram; every circular node represents a single neuron, and each arrow represents an input-output connection. Input data is passed between nodes after multiplication by the weights (w) and summed in each hidden layer node. The hidden layer data is then weighted and summed again before being passed to the output node, which uses an activation function to generate a numerical output.

ANNs are a machine learning paradigm based on the structure of biological nervous systems^{18,53}. Data enters an ANN through an input layer, and is fed-forward to subsequent hidden layers. Each hidden layer contains neurons (nodes) wherein each neuron sums weighted inputs from preceding layers and passes the sum through an activation function to generate an output. The output layer sums weighted inputs from the last hidden layer, again using an activation function to generate a numerical output. This process is depicted in Fig. 7. ANNs are often used in LIBS analysis as they traditionally have the capability to capture complex data relationships to yield classification or regression models from large input data sets¹¹⁻¹⁴.

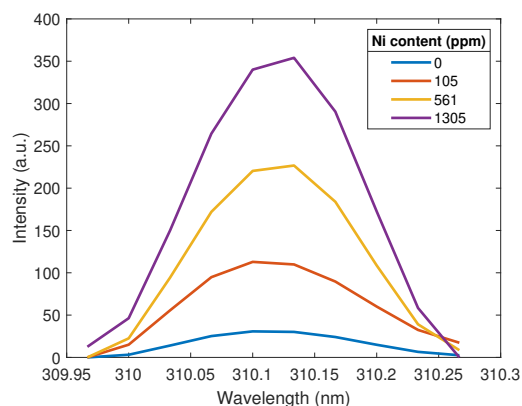
4 Results and Discussion

4.1 Univariate calibration curve

The Fe I 358 nm and Ni I 310 nm lines were selected as the basis of univariate calibrations as shown in Fig. 8 because they were the strongest lines available that were also interference free.



(a)



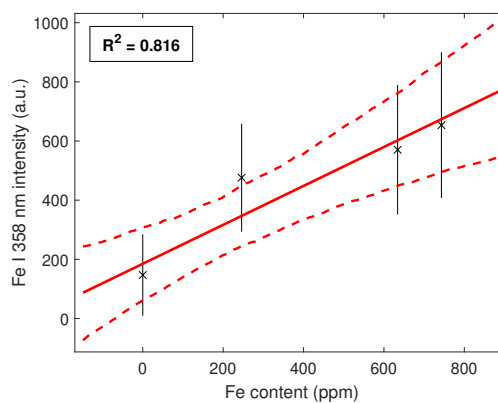
(b)

Fig. 8 Peak intensity of (a) Fe I 358 nm and (b) Ni I 310 nm emission lines at varying analyte concentrations.

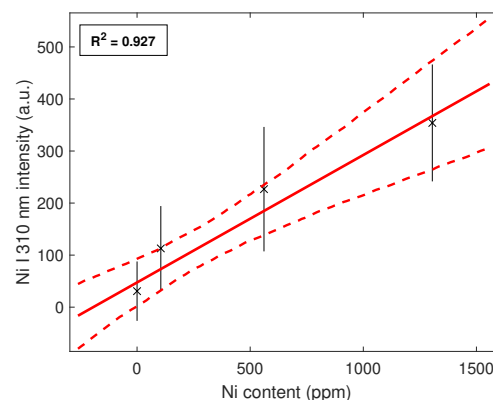
Nonetheless they are still minor peaks as all major peaks for iron and nickel suffered from interferences with Pu emissions. The selected emission line peak intensities for the four different concentrations of each element were extracted from the data, along with uncertainties propagated from standard deviation of the peak intensities between each shot. The custom MATLAB function *linfitxy()* was implemented to produce a linear regression which factored in the uncertainty of each data point, determined from the standard deviation of peak intensity between shots and statistical error propagation rules. The resulting linear regressions for Fe and Ni, along with R^2 values for each fit, are displayed in Fig. 9. The linear regressions to peak intensity were used to calculate a univariate LoD for each regression model. For the univariate case, the LoD is a simple relation described by Eq. 2, dependent on the standard deviation of the blank sample (σ) and the slope (a) of the regression fit.

$$LoD = \frac{3\sigma}{a} \quad (2)$$

Additionally, the $RMSE$ of each calibration was calculated according to Eq. 3, where N , y_i and \hat{y}_i represent the number of samples, predicted value, and actual value, respectively. While LoD provides a measure of model sensitivity, $RMSE$ provides the root of the sum of the squares of the model residuals, pointing to the pre-



(a)



(b)

Fig. 9 Calibration curve fits of (a) Fe I 358 nm and (b) Ni I 310 nm line peaks. The linear regression (solid red) is fit to the data points (black X) and the error bounds of the fit are marked by the dashed red lines. Uncertainty of each data point is noted with the vertical black lines; this was calculated by propagating the shot-to-shot deviation of the selected peak at each concentration.

dictive accuracy of the calibration. Calibrations with lower $RMSE$ values have less differences between predicted and actual data values, and are therefore more accurate.

$$RMSE = \sqrt{\frac{1}{N} \sum_{i=1}^n (y_i - \hat{y}_i)^2} \quad (3)$$

The fitting parameters for each calibration model and calculated are listed in Table 2, while the model LoD and $RMSE$ values are given in Table 3. The fit to the Ni peak yielded a better R^2 value than the Fe regression, but was marked by a poorer LoD. This is directly attributable to the lower slope of the Ni regression. The univariate LoD is directly dependent on the sensitivity of the measurements, quantified by the slope of the regression. A lower regression fit slope then correlates to a higher LoD and overall less sensitive model. It should also be noted that the univariate calibration LoDs are in the high hundreds of ppms; these quantities are unacceptable for accurately conducting a trace metal analysis in Pu. One potential underlying cause of the low sensitivities of these models that must be mentioned is a phenomenon known as

self-absorption, in which the plasma becomes optically opaque to analyte emission wavelengths at high concentrations, causing a lower than expected intensity to be recorded⁵⁴. This drives down the data points at higher concentrations and lowers the slope. When self absorption is corrected, or the data at higher concentrations is neglected, the regression slope to the lower concentration data points is often higher than initially calculated, lowering the LoD for trace analytes at lower concentration ranges. A previous study by Zhang *et al.* notes the fragility of implementing univariate methods for creating calibration curves due to susceptibility to fluctuations in laser energy and matrix effects in the sample⁵⁵. Sometimes these effects can be mitigated by normalizing the spectral internally to a particular strong emission line, however internal standard normalization often becomes less effective when analyzing a complex metal like plutonium with hundreds of convolved major emissions. This sheds some light as to the reasons for the high LoDs from these calibrations. Both regressions had *RMSE* values of the same order, with Ni markedly lower around 38. Ideally for a more accurate model, these *RMSE* values should be orders of magnitude lower than the range of target values for the regression. The clear underperformance of these simple univariate models stresses the need to implement chemometrics to generate more robust models which yield lower LoDs and prediction error values for better trace element quantification.

Table 2 Regression fitting parameters from the Fe and Ni univariate calibration models for the line $y = ax + b$.

Element	a	δa	b	δb	R^2
Fe	0.658	0.324	184.9	123.6	0.816
Ni	0.245	0.091	47.47	45.32	0.927

Table 3 LoD and RMSE values from the Fe and Ni univariate calibration models.

Element	$LoD(ppm)$	$RMSE$
Fe	640	95.2
Ni	700	38.1

Principal component regression (PCR)

The PCA algorithm was used to decompose the entire 145x23141 spectral emission data set into loadings and scores; the variance explained by the first 10 principal components is depicted in Fig. 10. The first three PCs explain over 95 percent of the variance of the data, a more than sufficient quantity needed to generate a regression. The first three PCs were kept and used to create a regression relating the transformed PC scores of components 1 through 3 to the mean centered concentrations of Fe and Ni in all the samples. Figs. 11a and 11b depict the generated predictive regression for each trace element, with the accompanying R^2 value for each fit.

The PCR method provided a poor fit to the Fe target data, and performed slightly better for the fit to the Ni target data. Analyzing the predictive accuracy of each model can be conducted

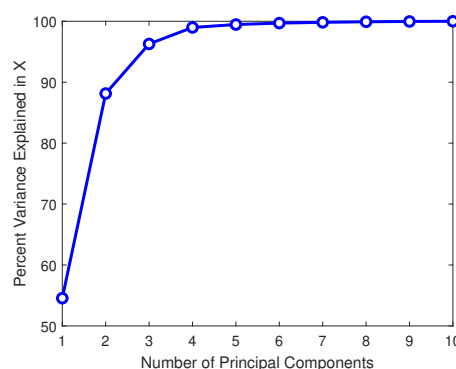
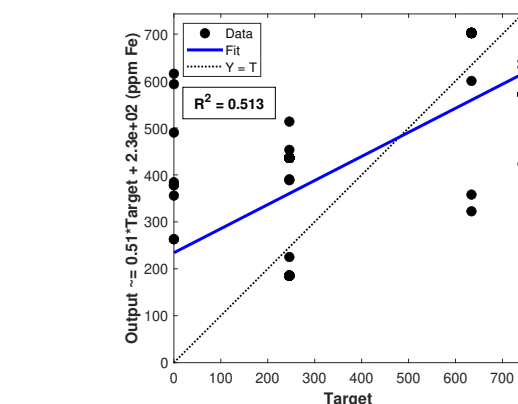
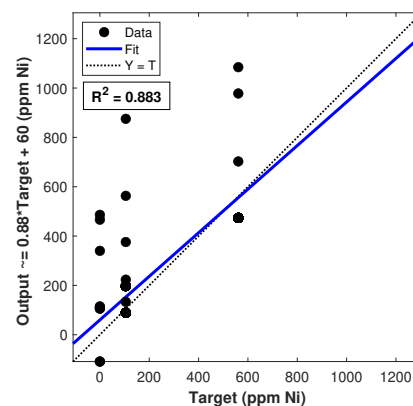


Fig. 10 Percentage of variance of the total data set explained by cumulative PCs. The more PCs used in the regression, the larger the percentage of the original variance explained by the model.



(a)



(b)

Fig. 11 PCR fits of a) Fe and b) Ni data. The fit (blue) to the data (black points) denotes how well the model output prediction of elemental concentration compared to the known target concentration.

by calculating the LoD of each regression. The methodology developed by Sun *et al.* for calculation of a multivariate regression model LoD was implemented in this work⁵⁶. Eqs. 4 and 5 describe the regression fit and LoD formula implemented. In Eq. 4, a and b respectively represent the intercept and slope of the regression fit line of the target concentration \hat{T} to the model output concentration \hat{O} . The standard deviation of a due to the dispersion of \hat{O} and the regression slope b were then extracted and used

to calculate LoD via Eq. 5. Thus, the LoD is a function of the sensitivity of the technique (b) and the accuracy of the regression model (σ_a). It should be explicitly noted that the calculated LoD does not yield a precise quantification of the amount of the trace element in the bulk sample. Rather, it represents the concentration of the element which must be present in the bulk for the chemometric model to determine presence of the trace element with 99% certainty.

$$\hat{O} = a + b \times \hat{T} \quad (4)$$

$$LoD(ppm) = \frac{3\sigma_a}{b} \quad (5)$$

Table 4 lists the regression fit parameters, R^2 , and calculated LoDs and RMSEs for each element. Although the LoD for Ni was comparable to the lower bound of the range of this trace metals in the samples, the result for Fe is markedly poorer at 340 ppm. This is directly caused by the poor PCR fit to the Fe target data, indicating that PCR may not be able to perform well enough to reliably analyze trace iron content in plutonium metal. One explanation for this disparity in achieved LoD could be that emissions from Fe interfere more with the Pu emissions in the spectra than Ni emissions do. Higher elemental and spectral interference may inhibit the PCA algorithm's ability to distinguish between the elements and provide a robust regression model. Overall, both PCR models displayed poor predictive accuracy as noted by their high RMSE values. These values are an order of magnitude higher than the corresponding univariate RMSEs. This trend is directly attributable to the unsupervised nature of the PCA technique; without target data to fit to the trends in spectral intensity variations, the predictive capability of the model is significantly diminished. These results conclude that PCA is not the ideal solution for analysis of complex spectral data, and a supervised chemometric technique is necessary.

Table 4 Regression fit parameters, R^2 , LoD and RMSE for PCR models.

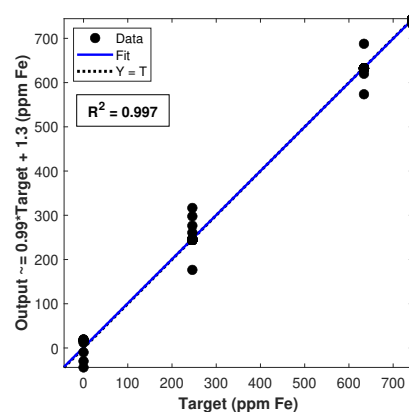
Element	a	b	R^2	LoD(ppm)	RMSE(ppm)
Fe	230	0.51	0.513	340	176
Ni	60	0.88	0.883	125	160

Partial-least squares regression (PLSR)

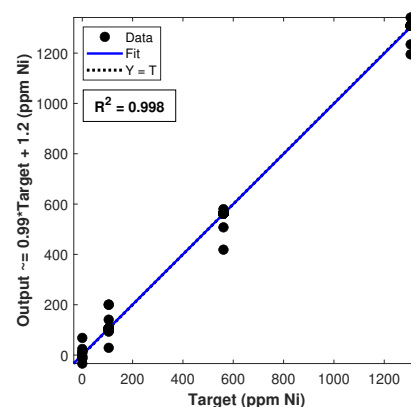
A PLS decomposition was performed on the complete spectral data set; a regression was constructed using the first 3 latent variables, which account for more than 95% of the original variance, to keep consistency with the PCR model. The regression fits and accompanying R^2 values are illustrated in Figs. 12 and 13. LoD and RMSE values were calculated for each fit according to the previously discussed methodology; these metrics along with the regression fit parameters are listed in Table 5.

Table 5 Regression fit parameters, R^2 , LoD and RMSE for PLSR models.

Element	a	b	R^2	LoD(ppm)	RMSE(ppm)
Fe	1.3	0.99	0.997	15	13.2
Ni	1.2	0.99	0.998	20	22.8



(a)



(b)

Fig. 12 PLSR fits of a) Fe and b) Ni data. The fit (blue) to the data (black points) denotes how well the model output prediction of elemental concentration compared to the known target concentration.

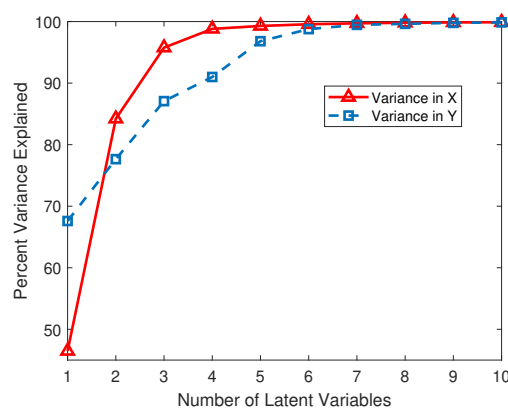


Fig. 13 Percent variance in total input (X) and target (Y) data explained by cumulative LVs of PLS model. Constructing a regression with more LVs yields a model explaining a higher portion of the total data variance.

The R^2 values indicate a nearly perfect correlation between the target and predicted analyte concentrations. Each model was able to achieve an LoD an order of magnitude lower than that of their

corresponding PCR fits, reaching the low 10s of ppm levels for both elements. This significant improvement in sensitivity is directly attributable to the high slopes of the regression fits to the PLS prediction data. Additionally, significant improvements in *RMSE* were made with this model when compared to the univariate and PCR methods, with the Fe regression reaching the low 10s of ppm levels for error. These values show promise that the PLS algorithm can accurately track small changes in spectral intensity caused by variations in trace metal content, and accurately represent these trends in a quantitative model. Overall, the PLSR models performed substantially better than the PCR models evaluated earlier, showing vastly increased sensitivity and higher predictive accuracy. To determine exactly why PLSR outperforms PCR to this degree, we examined the variance explained by each latent variable for each part of the data. Unlike PCA, PLS also generates variables explaining the covariances between the input (spectral data) and output (metal content); this is illustrated in Fig. 13. The first 3 LVs explain over 95 percent of the variance in X, but also account for about 85 percent of the variance in Y. The PLSR model uses the transformed data relating the input and output variables in the regression and is able to better quantify the relationships between spectral response and trace metal content. As a result, it generates better regression fits to the target data and yields lower LoDs for each element than the corresponding PCR models. These results indicate that a supervised learning technique is necessary to properly capture and quantify the relationship between spectral emission variations and trace metal content in the plutonium metal.

ANNs

A shallow feedforward neural network (FFNN) with 100 neurons in the hidden layer and a scaled conjugate gradient optimization function was built to perform regression fits of the data for both trace elements. This specific structure was chosen since it was applied in a previous study on Pu surrogate material spectra for detection of Si²³. A 60/20/20 % training/validation/testing split was applied to the full set of 145 spectra. Figs. 14 and 15 display the training (blue), validation (green), testing (red) and total (grey) regressions for Fe and Ni content determination. *R*² values for each elemental model and partition are listed in Table 6. The training and validation fits for Fe showed high *R*² values, but the test regression significantly underperformed with a poor *R*² of 0.492. This result provides a primary indication that the FFNN failed to generalize an accurate predictive model for new spectral data, despite achieving good fit metrics for the data during training and validation. Additionally, the FFNN test regression data for Fe yielded an LoD of 290 ppm, four times higher than the LoD of the PLSR for Fe, indicating significant underperformance for iron content prediction.

Table 6 *R*² values for ANN training, validation, test and total regression fits for each elemental model.

Element	Train	Validate	Test	Total
Fe	0.977	0.960	0.492	0.834
Ni	0.940	0.975	0.813	0.921

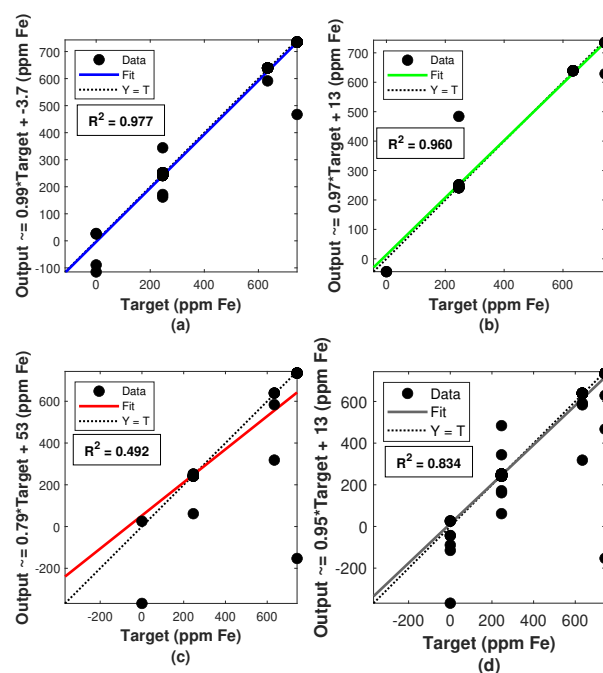


Fig. 14 FFNN a) training (blue), b) validation (green), c) testing (red) and d) total (grey) regression fits for Fe content prediction.

The FFNN regressions for Ni content prediction displayed the same issues as the model for Fe. Although the test data regression for Ni had an *R*² significantly higher than that of the Fe fit (0.813), it still yielded a poorer fit than the training and validation regressions. The test regression data and fit parameters yielded an LoD of 150 ppm for Ni, an improvement over the LoD for Fe but still higher than the 110 ppm LoD for Ni achieved by the PLSR model. These initial metrics indicate that the ANN architectures employed were not able to successfully generalize the trained models to test data; this is further investigated by examining the performance plot of each model.

Figs. 16a and 16b respectively illustrate the performance curves for the ANN models built for the Fe and Ni regressions over each training cycle (epoch). The blue, red, and green lines respectively note the mean-squared error (MSE) yielded by the model at a certain epoch for the training, validation, and test data. In both models, the test performance curve terminates at an MSE about an order of magnitude higher than the training and validation MSEs. This indicates the occurrence of overfitting; the model failed to generalize the results from training and validation to new data and could not generate accurate predictions for the test set. Further evidence of this behavior is listed in Table 7, which displays *RMSE* of the training set, root mean-squared error of cross validation (*RMSECV*) for the validation set, and root mean-squared error of prediction (*RMSEP*) of the test set. The model generates order of magnitude higher errors with the test data than with the training or validation set, indicating a failure to generalize the trends from the spectral information. Overfitting often plagues ANN based regression models when large and complex data sets are being passed for training and prediction.

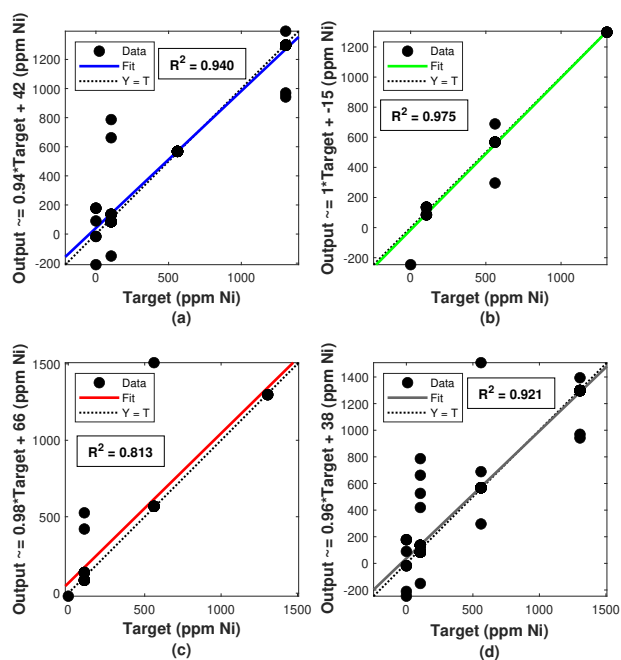


Fig. 15 FFNN a) training (blue), b) validation (green), c) testing (red) and d) total (grey) regression fits for Ni content prediction.

Table 7 Root mean-square errors for training, validation and testing ANN regression models for Fe and Ni. All error values are in ppm.

Element	RMSE	RMSECV	RMSEP
Fe	28.9	50.6	211
Ni	62.6	73.2	184

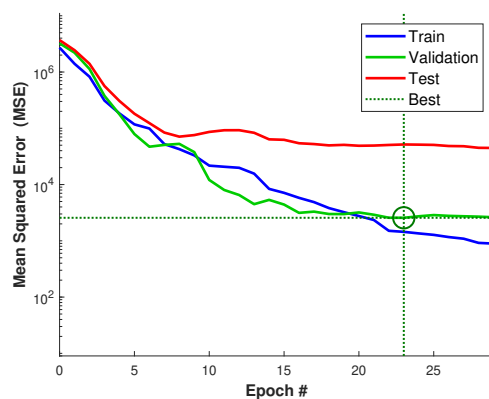
The behavior seen in the performance curve indicates that the ANN models are operating with low bias and high variance. This result indicates the need to implement methods such as hyperparameter tuning and regularization to increase bias and lower variance to overcome overfitting. The performance curve results also reflect the disparity between the R^2 values of the training and test regressions in Figs. 14 and 15. Combining the evidence of the poorer test regression fit and higher test MSE rendered by the Fe and Ni prediction models, it is clear that the chosen ANN architecture cannot produce an entirely reliable or robust model for concentration determination of these two trace metals. The test data regression fitting parameters and evaluation metrics for all ANN models are listed in Table 8.

Table 8 Regression fit parameters, R^2 , and LoD for ANN models.

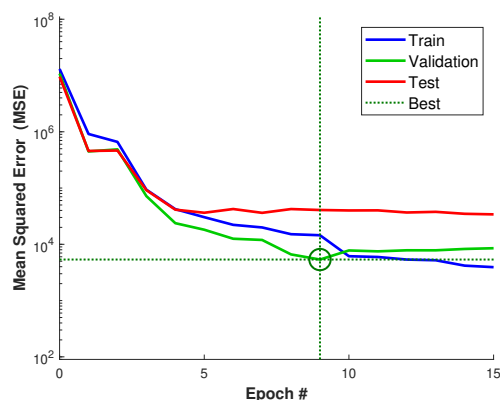
Element	a	b	R^2	LoD(ppm)
Fe	53	0.79	0.492	290
Ni	66	0.98	0.813	150

5 Conclusions

This study presents trace element quantification and LoD determination via portable LIBS for Pu alloys for the first time, using univariate analysis and three chemometric methods. Furthermore,



(a)



(b)

Fig. 16 Performance curves for a) Fe and b) Ni regressions denoting change in MSE for each ANN model during training (blue), validation (green) and testing (red) over each training cycle (epoch). The order of magnitude disparity between the end result of the test curve to the training curve indicates overfitting.

the results of this work yielded marked improvements to previous LoD determinations using handheld LIBS systems for analysis of uranium⁴⁶ and cerium-gallium alloys⁴⁸, proving the efficacy of chemometric methods for this problem. PLSR is determined to be the superior chemometric method for creating predictive regressions to determine trace metal concentrations, when compared to univariate, PCR and ANN methods. The PLSR method yielded LoDs of 15 and 20 ppm for Fe and Ni, respectively, along with RMSEs of 13.2 and 22.8 ppm, indicating a promising method for rapid chemical analysis of plutonium alloys. Univariate calibrations in complex matrices are subject to fluctuations in laser signal and sample matrix effects which can detrimentally affect the sensitivity and accuracy of the regression model. The unsupervised nature of PCR makes it less than ideal for this complex analytical spectroscopy problem, as it produces less accurate predictive models with poorer regression fits. The ANN architecture implemented in this work suffered from overfitting when creating regression models for Fe and Ni content, as determined by the order-of-magnitude difference in MSE between the training and test model performance. The overall results indicate that ANN methods struggle to produce entirely reliable and robust models

to quantitatively analyze the complex plutonium spectra.

It should be noted that PLSR still fails to reach the sub 10s of ppm threshold which has been achieved previously with full scale LIBS systems operating on less complex chemical matrices^{57–59}. Future endeavors for quantifying trace metals in Pu alloys could look to improve LoDs further by either attempting other novel machine learning paradigms as have been proposed for Pu surrogates²³, or by enhancing the spectral resolvability by improving the experimental setup to better replicate laboratory conditions. Additionally, future work with these machine learning models will examine the optimization of various hyperparameters, such as the number of neurons, optimization function, and learning speed coefficient used in the ANN, to maximize the performance of the prediction models implemented for this problem. Lastly, this work can be expanded to analyze a larger range of trace elements relevant to Pu production, such as gallium, silicon, neptunium, and americium. Analyzing a larger amount of trace impurities and decay product elements will yield better insight into how different models perform and behave for analysis of different elements.

Conflicts of interest

There are no conflicts to declare.

Acknowledgements

The authors would like to thank the Defense Threat Reduction Agency's Nuclear Technologies Directorate for sponsorship of this research. Additionally, this project is supported by LANL internal funding provided by Plutonium Sustainment and Material Recycle and Recovery. This work was reviewed, approved and released with the LA-UR-21-20399.

Notes and references

- 1 P. Torriano, L. Collins and K. Morton, *Laser Spectroscopy for Sensing*, Woodhead Publishing, 2014, pp. 125 – 164.
- 2 S. M. Clegg, E. Sklute, M. D. Dyar, J. E. Barefield and R. C. Wiens, *Spectrochimica Acta Part B: Atomic Spectroscopy*, 2009, **64**, 79 – 88.
- 3 V. K. Unnikrishnan, K. S. Choudhari, S. D. Kulkarni, R. Nayak, V. B. Kartha and C. Santhosh, *RSC Adv.*, 2013, **3**, 25872–25880.
- 4 S. Moncayo, L. Duponchel, N. Mousavipak, G. Panczer, F. Trichard, B. Bousquet, F. Pelascini and V. Motto-Ros, *J. Anal. At. Spectrom.*, 2018, **33**, 210–220.
- 5 P. Yaroshchik, D. L. Death and S. J. Spencer, *J. Anal. At. Spectrom.*, 2012, **27**, 92–98.
- 6 A. K. Pathak, R. Kumar, V. K. Singh, R. Agrawal, S. Rai and A. K. Rai, *Applied Spectroscopy Reviews*, 2012, **47**, 14–40.
- 7 X. Li, Z. Wang, S.-L. Lui, Y. Fu, Z. Li, J. Liu and W. Ni, *Spectrochimica Acta Part B: Atomic Spectroscopy*, 2013, **88**, 180 – 185.
- 8 P. Heraud, B. R. Wood, J. Beardall and D. McNaughton, *Journal of Chemometrics*, 2006, **20**, 193–197.
- 9 R. S. Harmon, R. R. Hark, C. S. Throckmorton, E. C. Rankey, M. A. Wise, A. M. Somers and L. M. Collins, *Geostandards and Geoanalytical Research*, 2017, **41**, 563–584.
- 10 R. B. Anderson, J. F. Bell, R. C. Wiens, R. V. Morris and S. M. Clegg, *Spectrochimica Acta Part B: Atomic Spectroscopy*, 2012, **70**, 24 – 32.
- 11 J. El Haddad, M. Villot-Kadri, A. Ismael, G. Gallou, K. Michel, D. Bruyère, V. Laperche, L. Canioni and B. Bousquet, *Spectrochimica Acta Part B: Atomic Spectroscopy*, 2013, **78–79**, 51–57.
- 12 E. C. Ferreira, D. M. Milori, E. J. Ferreira, R. M. Da Silva and L. Martin-Neto, *Spectrochimica Acta Part B: Atomic Spectroscopy*, 2008, **63**, 1216 – 1220.
- 13 P. Inakollu, T. Philip, A. K. Rai, F.-Y. Yueh and J. P. Singh, *Spectrochimica Acta Part B: Atomic Spectroscopy*, 2009, **64**, 99 – 104.
- 14 A. Koujelev and S.-L. Lui, in *Artificial Neural Networks for Material Identification, Mineralogy and Analytical Geochemistry Based on Laser-Induced Breakdown Spectroscopy*, 2011.
- 15 J. Moros, J. Serrano, C. Sánchez, J. Macías and J. J. Laserna, *J. Anal. At. Spectrom.*, 2012, **27**, 2111–2122.
- 16 H. Fu, J. Jia, H. Wang, Z. Ni and F. Dong, *Calibration and Validation of Analytical Methods - A Sampling of Current Approaches*, IntechOpen, 2017.
- 17 Z.-B. Cong, L.-x. Sun, Y. Xin, Y. Li and L.-f. Qi, *Journal of Computer and Communications*, 2013, **01**, 14–18.
- 18 D. Larose and C. Larose, *Data Mining and Predictive Analysis*, Wiley, 2015.
- 19 T. F. Boucher, M. V. Ozanne, M. L. Carmosino, M. D. Dyar, S. Mahadevan, E. A. Breves, K. H. Lepore and S. M. Clegg, *Spectrochimica Acta Part B: Atomic Spectroscopy*, 2015, **107**, 1 – 10.
- 20 Y. Yang, C. Li, S. Liu, H. Min, C. Yan, M. Yang and J. Yu, *Anal. Methods*, 2020, **12**, 1316–1323.
- 21 P. K. Tiwari, S. Awasthi, R. Kumar, R. K. Anand, P. K. Rai and A. K. Rai, *Lasers in Medical Science*, 2018, **33**, 263–270.
- 22 J. E. Barefield, E. J. Judge, K. R. Campbell, J. P. Colgan, D. P. Kilcrease, H. M. Johns, R. C. Wiens, R. E. Mcinroy, R. K. Martinez and S. M. Clegg, *Spectrochim. Acta B*, 2016, **120**, 1–8.
- 23 A. P. Rao, P. R. Jenkins, J. D. Auxier and M. B. Shattan, *J. Anal. At. Spectrom.*, 2021, 399–406.
- 24 S. I. for Transactinium Science, *Actinide Research Quarterly*, 2008.
- 25 S. S. Hecker, *Plutonium and Its Alloys*, 2000.
- 26 D. Clark, S. Hecker, G. Jarvinen and M. Neu, *Chemistry of the Actinide and Transactinide Elements*, Springer, Dordrecht, 2008.
- 27 S. I. for Transactinium Science, *Actinide Research Quarterly*, 2012.
- 28 P. Söderlind, F. Zhou, A. Landa and J. Klepeis, *Scientific Reports*, 2015, **5**, 15958.
- 29 S. S. Hecker, *JOM*, 2003, **55**, 13–19.
- 30 M. Steinzig and F. H. Harlow, *MRS Proceedings*, 1999, **538**,.
- 31 M. Krachler and R. Alvarez-Sarandes, *Microchemical Journal*, 2016, **125**, 196 – 202.
- 32 E. Simon, A. Vidic, M. Braun, I. Fabian and B. Tothmeresz, *Environ Sci Pollut Res Int*, 2012, 917–24.

- 1 33 R. Falciani, E. Novaro, M. Marchesini and M. Gucciardi, *J.*
2 *Anal. At. Spectrom.*, 2000, **15**, 561–565.
- 3 34 Radboud, *General Instrumentation*, [https://](https://www.ru.nl/science/gi/facilities-activities/elemental-analysis/icp-oes/)
4 [www.ru.nl/science/gi/facilities-activities/](https://www.ru.nl/science/gi/facilities-activities/elemental-analysis/icp-oes/)
5 [elemental-analysis/icp-oes/](https://www.ru.nl/science/gi/facilities-activities/elemental-analysis/icp-oes/), 2018, Accessed on 2019-
6 04-16.
- 7 35 G. L. Donati, R. S. Amais and C. B. Williams, *J. Anal. At. Spec-*
8 *trom.*, 2017, **32**, 1283–1296.
- 9 36 D. Hahn and N. Omenetto, *Applied Spectroscopy*, 2010, **64**,
10 335–66.
- 11 37 D. W. Hahn and N. Omenetto, *Appl. Spectrosc.*, 2012, **66**, 347–
12 419.
- 13 38 G. Guo, G. Niu, Q. Shi, Q. Lin, D. Tian and Y. Duan, *Anal.*
14 *Methods*, 2019, **11**, 3006–3013.
- 15 39 N. Yang, N. Eash, J. Lee, M. Martin, Y.-S. Zhang, F. Walker
16 and J. E. Yang, *Soil Science*, 2010, **175**, 447–452.
- 17 40 B. Connors, A. Somers and D. Day, *Applied Spectroscopy*, 2016,
18 **70**, 810–815.
- 19 41 E. Bellou, N. Gyftokostas, D. Stefas, O. Gazeli and S. Couris,
20 *Spectrochimica Acta Part B: Atomic Spectroscopy*, 2020, **163**,
21 105746.
- 22 42 B. T. Manard, M. F. Schappert, E. M. Wylie and G. E. McMath,
23 *Anal. Methods*, 2019, **11**, 752–759.
- 24 43 Y. Wu, M. Gragston, Z. Zhang, P. S. Hsu, N. Jiang, A. K. Pat-
25 naik, S. Roy and J. R. Gord, *Combustion and Flame*, 2018,
26 **198**, 120 – 129.
- 27 44 A. K. Patnaik, Y. Wu, P. S. Hsu, M. Gragston, Z. Zhang, J. R.
28 Gord and S. Roy, *Opt. Express*, 2018, **26**, 25750–25760.
- 29 45 SciAps, *SciAps Z Series Spec Sheet*, 2016, [https:](https://www.sciaps.com/wp-content/uploads/2016/02/SciAps-Z-Series_Spec-Sheet.pdf)
30 [//www.sciaps.com/wp-content/uploads/2016/02/](https://www.sciaps.com/wp-content/uploads/2016/02/SciAps-Z-Series_Spec-Sheet.pdf)
31 [SciAps-Z-Series_Spec-Sheet.pdf](https://www.sciaps.com/wp-content/uploads/2016/02/SciAps-Z-Series_Spec-Sheet.pdf).
- 32 46 M. B. Shattan, D. J. Miller, M. T. Cook, A. C. Stowe, J. D.
33 Auxier, C. Parigger and H. L. Hall, *Appl. Opt.*, 2017, **56**, 9868–
34 9875.
- 35 47 B. T. Manard, E. M. Wylie and S. P. Willson, *Applied Spec-*
36 *troscopy*, 2018, **72**, 1653–1660.
- 37 48 A. P. Rao, M. T. Cook, H. L. Hall and M. B. Shattan, *Atoms*,
38 2019, **7**.
- 39 49 G. Long and J. Winefordner, *Analytical Chemistry - ANAL*
40 *CHEM*, 2008, **55**.
- 41 50 D. Syvilay, N. Wilkie-Chancellier, B. Trichereau, A. Texier,
42 L. Martinez, S. Serfaty and V. Detalle, *Spectrochimica Acta Part*
43 *B: Atomic Spectroscopy*, 2015, **114**, 38 – 45.
- 44 51 A. Ismaël, B. Bousquet, K. M.-L. Pierrès, G. Travaillé, L. Can-
45 ioni and S. Roy, *Applied Spectroscopy*, 2011, **65**, 467–473.
- 46 52 A. Rao, *MSc thesis*, Air Force Institute of Technology, Wright-
47 Patterson AFB, 2020.
- 48 53 S. Haykin, *Neural Networks: A Comprehensive Foundation*,
49 Prentice Hall, 1999.
- 50 54 F. Rezaei, G. Cristoforetti, E. Tognoni, S. Legnaioli, V. Palleschi
51 and A. Safi, *Spectrochimica Acta Part B: Atomic Spectroscopy*,
52 2020, **169**, 105878.
- 53 55 T. Zhang, H. Tang and H. Li, *Journal of Chemometrics*, 2018,
54 **32**, e2983.
- 55 56 C. Sun, Y. Tian, L. Gao, Y. Niu, T. Zhang, H. Li, Y. Zhang,
56 Z. Yue, N. Delepine-Gilon and J. Yu, *Scientific Reports*, 2019,
57 **9**, 11363.
- 58 57 Y. Lee, S.-W. Oh and S.-H. Han, *Applied spectroscopy*, 2012,
59 **66**, 1385–96.
- 60 58 S. Ma, Y. Tang, Y. Ma, Y. Chu, F. Chen, Z. Hu, Z. Zhu, L. Guo,
X. Zeng and Y. Lu, *Opt. Express*, 2019, **27**, 15091–15099.
- 59 59 A. Khumaeni, W. S. Budi, K. Kurihara, H. Kurniawan and
K. Kagawa, *Heliyon*, 2020, **6**, e04670.